Review Article

Nano Research
2019, 12(9): 2126–2139

ISSN 1998-0124 CN 11-5974/O4
https://doi.org/10.1007/s12274-019-2408-6

Recent progress on *in situ* characterizations of electrochemically intercalated transition metal dichalcogenides

Sajad Yazdani[1,2,§], Milad Yarali[1,2,§], and Judy J. Cha[1,2,§] (✉)

[1] *Department of Mechanical Engineering and Materials Science, Yale University, New Haven, CT 06511, USA*
[2] *Energy Sciences Institute, Yale University West Campus, West Haven, CT 06516, USA*
[§] *Sajad Yazdani, Milad Yarali and Judy J. Cha contributed equally to this work.*

Received: 20 December 2018 / **Revised:** 21 March 2019 / **Accepted:** 8 April 2019

ABSTRACT

Layered transition metal dichalcogenides (TMDCs) have been extensively studied owing to their unique physical and chemical properties. Weak van der Waals (vdW) interactions between the stacking layers of TMDCs allow intercalation of various species including monovalent alkali, divalent alkaline earth and multivalent metal ions, zero-valent transition metals, as well as organic molecules, all of which can drastically alter fundamental properties of the TMDCs. The urge to understand the phenomena and the desire to exploit them for applications have inspired a great deal of investigations. A large portion of the mystery has been unveiled over the past decade of intense research; however, many questions remain open and require further explorations. This review is concerned with investigations on structural and electronic evolution of TMDCs driven by electrochemically controlled intercalations. Herein, we aim to survey the recent advances and experimental platforms for monitoring the intercalation processes *in situ* by utilizing nanodevices. In addition, several inquiries and prospects are outlined in a broader context for future avenues of studies.

KEYWORDS

transition metal dichalcogenides, electrochemical intercalation, *in situ* characterizations, transmission electron microscopy (TEM), magnetotransport measurements

1 Introduction

The drive to tune the physical and chemical properties of layered TMDCs has pushed scientific and engineering communities to develop new and ever-improving processes, tools, and methodologies over the past half-century. Examples include dimensional sizing [1, 2], intercalation [3], heterostructures and alloying [4], external field tuning [5, 6], and strain engineering [7], among which intercalation of foreign species has occupied a unique space in terms of its ability to substantially induce charge transfer and structural change in the hosting TMDCs. The advances in physical realization, manipulation, and characterization of atomically thin two-dimensional (2D) materials in the past two decades have fueled vibrant research activities with renewed interest to revisit the early studies of intercalation in the bulk form of the layered materials. The layered intercalation compounds exhibit novel heterostructures and a variety of exotic electronic properties ranging from superconductivity to magnetism [8–14]. Intercalation has also been utilized to manipulate optical and thermal properties of hosting layered materials by changing the band filling state and the Fermi level, and perturbation in the phonon propagation. This makes the intercalated 2D materials suitable to be implemented in the functional optoelectronic devices as well as energy conversion applications such as thermoelectrics and photovoltaics [15–24]. The intercalation-induced phase change has provided a unique approach to increase charge conductivity and optimize the catalytic activities of layered materials for enhanced and cost-efficient hydrogen evolution reaction (HER) [25–29]. Intercalation of guest species enlarges the interlayer space of the hosting lattice, thus making the electrochemical active sites more accessible with lower diffusion barrier. This is advantageous for sustainable energy storage systems such as supercapacitors, metal ion batteries and thermoelectrics [30–41]. Recent real-time investigations of intercalations have led to insightful discoveries, advancing our understanding of the phenomena. The aim of this review is to survey the current state of the literature on *in situ* structural and electronic property characterizations, and to advocate prospects for future investigations. For other topics including fundamentals and properties of layered TMDCs and intercalations, interested readers are referred to previously published review articles [42–46]. Recent works on the electrochemically controlled intercalation of layered materials are summarized in Table 1. This survey indicates that there are still many topics that need to be explored given the diversity of the layered material systems and heterostructures, intercalants and the characterization methods.

2 Crystal structure and polymorphs of TMDCs

Similar to graphite, TMDCs can form layered structures. TMDCs consist of metal atoms (M) from groups 4–7 and 10 such as Ti, Zr, Hf, V, Nb, Ta, Mo, W, Tc, Re, and Pt, bonded to chalcogens (X) from group 16 including S, Se and Te. The general formula for a TMDC can be expressed as MX_2 assuming M^{4+} and X^{2-} oxidation states. Each metal atom is hexagonally packed in between two layers of chalcogens through the strong covalent bonding, forming a single layer of X–M–X with a typical thickness of ~ 6–7 Å [43]. The electron configuration of chalcogens in the valence shell can be expressed as $ns^2p_x^1p_y^1p_z^2$

Address correspondence to judy.cha@yale.edu

Table 1 Summary of the electrochemically controlled *in situ* intercalation studies in layered materials

Intercalation host	Intercalants	*In situ* characterization method	References
MoS_2 nanosheets	Li^+	TEM	[47]
	Li^+	Optoelectronic measurements, TEM	[32]
	Li^+	Optoelectronic measurements	[48]
	Li^+	Thermal conductance studies	[22]
	Na^+	TEM	[49, 50]
	Li^+, Na^+, K^+	Optoelectronic measurements	[51]
Bilayer graphene	Li^+	TEM	[52]
		Electrical transport measurements	[53]
Ultrathin graphite	Li^+	Optoelectronic measurements	[18]
Graphene/h-BN heterostructure	Li^+	Electrical transport measurements	[54]
MoS_2, $MoSe_2$, graphene, h-BN heterostructures	Li^+	Magnetotransport measurements	[55]
Nanoscale Bi_2Se_3	Cu^0	TEM, low-temperature transport	[56]

implying that the p orbital embodies two unpaired electrons along with a lone-pair of electrons. The unpaired p orbitals participate in the covalent bonding between the chalcogen and the metal atoms whereas the lone-pair electrons are chemically inactive [57]. It is assumed that the surface of the layer is terminated by the lone-pair electrons located on sp^3-hybridized orbitals [57], allowing the layered nature of TMDCs due to the lack of dangling bonds on the surface. The metal coordination has been found to be either trigonal prismatic (D_{3h}, 1H) (e.g., MoS_2, NbS_2) or octahedral (O_h,) also known as trigonal antiprismatic (D_{3d}, 1T) (e.g., HfS_2) [42, 43, 57]. In the trigonal prismatic arrangement, X atoms are stacked over each other whereas in the octahedral symmetry the X atoms are staggered. Normally, group 4 and most of group 5 metals have octahedral structures while group 6 metals take the trigonal prismatic coordination. In group 7, distorted octahedral structures can be found while in group 10, all TMDCs exist in octahedral arrangements [57]. Such a variation in coordination was explored by Kertesz and Hoffmann [58] using band calculations of electronic structure stabilities. Their analysis suggested that for d^0 electron count complexes (e.g., $TiSe_2$), the octahedral structure is more stable. By filling the lowest d band however, the trigonal-prismatic structure begins to become more favorable, with the effect reaching its maximum around d^2 (e.g., MoS_2). As the d band electron count further increases to d^3, the octahedral coordination is once again more favorable [58] although distorted to give chains of metal-metal bonded diamonds [58]. Examples include the octahedral preference in TiS_2 with d^0, trigonal-prismatic stability in MoS_2 with the d^2 electron count, and distorted octahedral in $ReSe_2$ (d^3).

Bulk TMDCs can exhibit a variety of stacking polymorphs [43]. 1T with a tetragonal symmetry, 2H with a hexagonal symmetry, and 3R with a rhombohedral symmetry are the most common structural polytypes (stacking sequences) [3] in which the unit cell consists of one, two and three X–M–X single layers, respectively. Other polymorphs can be found in Ref. [57]. It is worth mentioning that the nomenclatures 2H and 3R are still widely used to refer to single layer and bilayer stacking polytypes, respectively, even though the numbers hint to 2 and 3 layers. Figure 1 illustrates the high-symmetry stacking sequences for bilayer and trilayer TMDCs. Among the five high-symmetry stacking patterns of the bilayer, two eclipsed AA′ (2H in bulk) and AB (3R in bulk) are stable and normally found. As described by Liang et al. [59], the AA′ (2H) stacking corresponds to M in one layer located on top of X in another layer (eclipsed with M over X). An AA stacking (M over M and X over X) has not been found to be stable in a bilayer MX_2. AB (3R) corresponds to M in one layer staggered over X in the other layer. AB′ (staggered with M over M) and A′B (staggered with X over X) are predicted to be metastable. In the trilayer, four types of stacking patterns can be proposed: AA′A, ABA, ABC and AA′B where AA′A and ABC correspond to the 2H and 3R stacking while

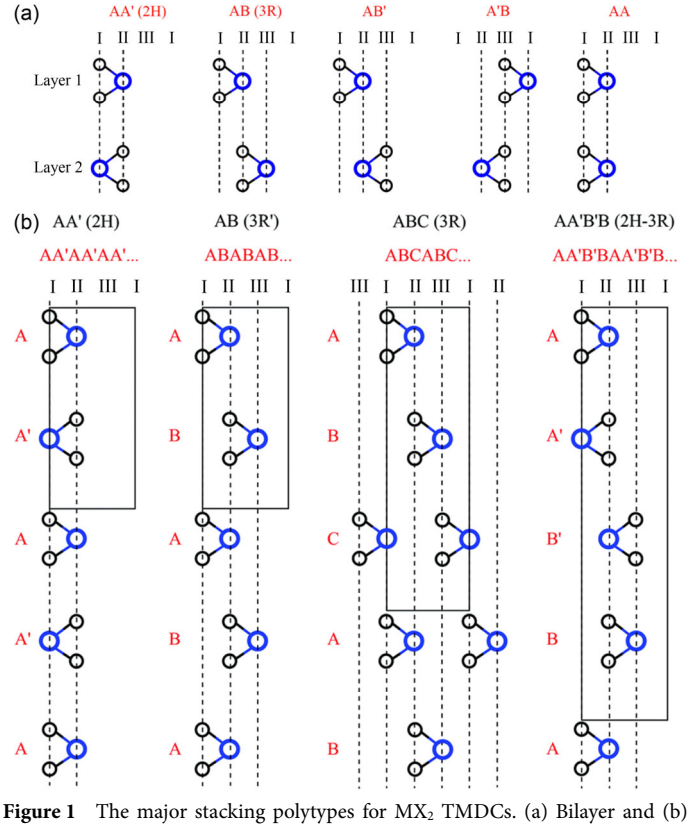

Figure 1 The major stacking polytypes for MX_2 TMDCs. (a) Bilayer and (b) multilayer structures. The large blue circles represent metal atoms (M) and the smaller black circles show the chalcogen atoms (X). Each letter is an indication of one atomic layer. The dashed lines show the atomic coordinates on the basal planes: I: 0, 0; II: 1/3, 2/3; III: 2/3, 1/3. The solid rectangles show the unit cells of the structures. Reprinted with permission from Ref. [59], © Royal Society of Chemistry 2017.

AA′B′ is a mixture of 2H and 3R polytypes [59].

Intercalation of foreign species has been shown to cause reversible structural changes in layered materials. Since material properties are dependent on structures, this has attracted intense investigations to identify pathways to use intercalation as a tool for tuning material properties [45, 46]. However, less attention has been paid to understand the evolution and kinetics of structural changes induced by intercalation. Several works [47, 49, 50, 60] have used nanodevices in conjunction with transmission electron microscopy (TEM) to observe the kinetics of intercalations in MoS_2. Although many interesting results have been reported, there remain unexplored realms and open questions that need to be investigated. Studying the kinetics of intercalation can give us a better understanding of the nature of intercalation, forces and interactions involved. Thorough

inspection of structural evolution can pave the way for consequent property change explorations.

3 Intercalation-induced structural changes and kinetics in TMDCs

The large vdW gap in TMDCs allows insertions of many foreign atoms and molecules. The intercalants occupy interstitial sites in the gap, and in most cases the process involves charge transfers between the intercalants and host TMDCs [42]. Alkali and alkaline earth metal ions, zero-valent transition metals, and organic species have been intercalated in TMDCs [46]. Intercalation of long organic molecules can effectively enhance the gap between the layers whereas insertion of alkali metal ions can replace the weak forces between layers with strong Coulombic interactions. Previously reported intercalants are electron donors; an electron acceptor intercalation can be hindered by Coulombic repulsion between the ionized acceptor and the neighboring chalcogen layers carrying an effective negative charge [42].

Octahedral and tetragonal interstitial sites are speculated as occupant sites for intercalants, which are surrounded by six and four nearest chalcogen atoms, respectively. The octahedral sites have been suggested to be more favorable for alkali metal intercalants such as Li^+ [61] and Na^+ [61, 62], whereas Ag ions have been found to occupy both the octahedral and tetrahedral sites [42]. It has been observed that intercalation of alkali metal ions Li^+, Na^+ or K^+ can induce structural phase transitions. For instance, for group 6 TMDCs, such as MoS_2 and WS_2, a phase transition from 2H to 1T occurs by chemical intercalation [3, 63, 64]. This phase transition is of interest as the octahedral 1T coordination does not form naturally in these materials. In addition, the structure can retain the 1T arrangement even after the reduction of the intercalants [65–67]. The 2H to 1T phase transition in MoS_2 can be explained by the band calculations of the phase stability [58]. Assuming a complete charge transfer from the alkali metal, the electron count increases from d^2 to d^3 allowing the octahedral geometry (1T) to be more favorable [43, 57, 58, 64]. For TaS_2, Li^+ intercalation triggers a reverse phase transition from 1T to 2H [68], which can be explained by changing from the d^0 to d^1 configuration and destabilizing the 1T octahedral phase. Fan and Li et al. [61] suggested that the energy gain for the electron transfer from Li^+ and Na^+ into the empty space above the Fermi level of pristine MX_2 can be used as a descriptor for the voltage of intercalated compounds. Their calculation predicted the voltage for a fully intercalated MoX_2 and WX_2 (less than 1 V) to be lower than those of NbX_2 and TaX_2 (1.5 V).

In group 6 TMDCs, the 1T system is a metastable phase and can undergo a phase transition to the 2H upon heating [69]. The 1T phase in the restacked WS_2 was found to be much more stable than that in the restacked MoS_2 [70]. In MoS_2, the metastable 1T phase can form the more stable 1T' by distortion of the structure [70–74]. Formation of several types of superlattices for the chemically exfoliated and restacked MoS_2 and WS_2 materials has been observed, mostly by using selected area electron diffraction (SAED) studies. In the *ab* plane, various superlattices including $2a \times a$ zigzag chain clusters, $2a \times 2a$ diamond structures, and triangular $\sqrt{3}a \times \sqrt{3}a$ super lattices have been reported [71, 72, 75–82]. The $2a \times a$ superlattice can be described by an orthorhombic $\sqrt{3}a \times a$ structure as it can be obtained by a triplet of three $\sqrt{3}a \times a$ rotated 120° relative to one another [75].

3.1 Structural evolution of Li^+ intercalation in MoS_2 nanosheets

One common configuration to perform *in situ* TEM characterizations of intercalation is to use a Li/Li_2O/working electrode (intercalation host) open-cell electrochemical system. A Li or Na metal is scratched on a tungsten tip; then the tip is exposed to air for a short time to oxidize the outer surface of the metal, acting as a solid electrolyte. A piezo controller is used to manipulate the tip against the TMDC sample. Using this method, Wang and co-workers [47] observed that SAED patterns assigned to the $2a \times 2a$ superlattice appeared in MoS_2 after 1 s of the Li^+ intercalation. After 6 s, new diffraction spots assigned to Li_2S appeared, and finally after 120 s, the patterns were converted to an amorphous Li_2S without any remaining superlattice signature. During intercalation, Bragg spots along the (001) attributed to the 1T became sharp and intense. The 2H and 1T phases exhibited the same major diffraction features, and intensity profiles were tracked to distinguish them. By monitoring the change in lattice parameters of the intercalated MoS_2, they noticed that the lattice along *a*-axis expanded slowly, whereas the dimension in the *c*-axis direction increased from 12.3 to 14 Å. During the intercalation, a wavy reaction front, propagating across the nanosheet, was observed (Figs. 2(a)–2(d)). Regions before the wavy front were indexed to the 2H phase whereas 1T phase SAED patterns were detected from the same area after the wavy front passed by. A buffer zone consisting of wavy periodic structures and distortion areas full of slip dislocations with elongated diffraction spots was also detected

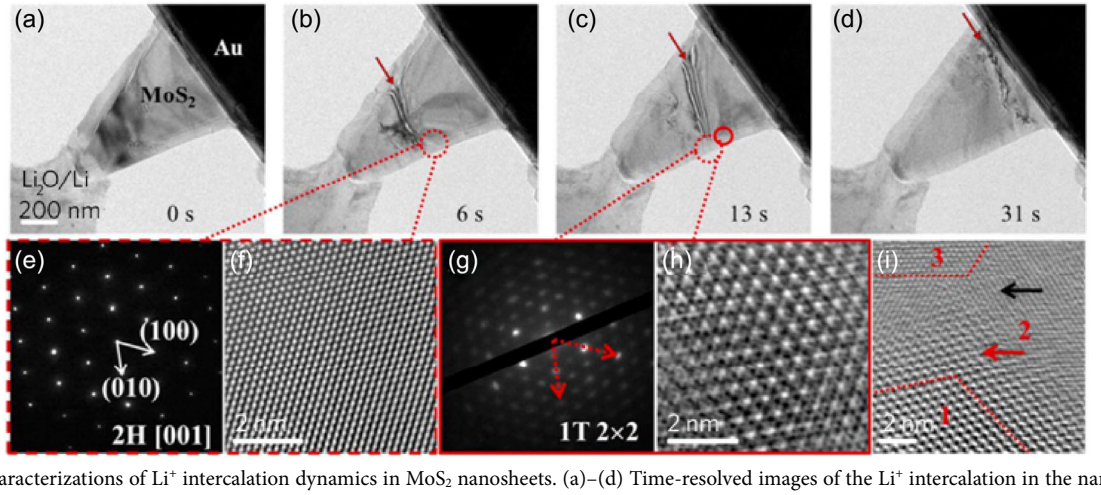

Figure 2 TEM characterizations of Li^+ intercalation dynamics in MoS_2 nanosheets. (a)–(d) Time-resolved images of the Li^+ intercalation in the nanosheet. The wavy region indicates the reaction front, and was attributed to sliding of slabs due to the 2H to 1T phase transition. The corresponding SAED and fast Fourier transform (FFT) patterns of the area marked by the red circles: before ((e) and (f)) and after ((g) and (h)) the passing of the wavy front. (i) HRTEM image of the phase boundary region showing: (1) the intercalated part with a superlattice structure, (3) the pristine and (2) the buffer area with dislocations. Reprinted with permission from Ref. [47], © American Chemical Society 2014.

(Fig. 2(i)). In the intercalated region a variety of $2a \times 2a$, $\sqrt{3}a \times a$, $2a \times a$, $a \times a$, and $\sqrt{3}a \times \sqrt{3}a$ microdomain superlattices were observed [47].

3.2 Structural evolution of Na^+ intercalation in MoS_2 nanosheets

Similar to Wang et al. [47], Gao and co-workers [49] used an open cell consisting of $Na/NaO_x/MoS_2$ nanosheets to investigate the dynamics of Na^+ intercalation under TEM, *in situ*. The SAED and FFT patterns indicated the formation of $2a \times 2a$ superlattice structures with a ~ 2 nm-wide phase boundary between the pristine and intercalated regions (Figs. 3(a)–3(d)). By monitoring the expansion of the intercalated regions (Fig. 3(e)), a reaction rate of ~ 3–7 $nm \cdot s^{-1}$ (corresponding to 10–50 $nm^2 \cdot s^{-1}$) was estimated, which was more sluggish than 30–70 $nm \cdot s^{-1}$ estimated for the case of Li ion intercalation [49] (Fig. 3(g)). The slow reaction was attributed to the larger ionic radius of Na^+ (1.16 Å) compared to that of Li^+ (0.76 Å) [83]. These diffusion rates of the reaction front are much lower than the previously measured diffusion coefficient of 5×10^5 $nm^2 \cdot s^{-1}$ for Li^+ intercalation in Li_xTiS_2, $0.0 < x < 1$ at room temperature [42, 84]. In contrast to the Li^+ intercalation, no lattice expansion was observed in the case of Na^+ intercalation, which was attributed to the strain release through formation of cracks.

Huang and Bai et al. [50] reported the phase transition from 2H-$Na_{0.5}MoS_2$ to 1T-$Na_{0.5}MoS_2$ using electrochemically controlled intercalation under TEM, *in situ*. At $Na_{0.25}MoS_2$, the first intermediate superlattice was assigned to the $2a \times \sqrt{3}a$ orthogonal structure relative to the 2H phase. The critical stoichiometric ratio of Na to Mo for the superlattice was obtained based on the simulation of the experimental SAED patterns showing three $2a \times \sqrt{3}a$ equivalent arrangements in a 6-fold symmetry. With the assumption of a uniform distribution of the intercalants in the interlayers, the ratio was taken to be 1 to 4 ($x = 0.25$). Further intercalation showed the appearance of $2a \times 2a$ along with $2a \times \sqrt{3}a$ superstructures. Two similar sets of diffraction spots were observed with different intensity profiles, which were assigned to 2H $Na_{0.5}MoS_2$ and 1T $Na_{0.5}MoS_2$. Unlike the intensity profiles obtained from the 2H $Na_{0.5}MoS_2$ diffraction patterns, the $\{11\bar{2}0\}$ spots were more intense than $\{10\bar{1}0\}$ in 1T $Na_{0.5}MoS_2$ (Fig. 4).

4 Electronic structure characterizations of TMDCs

The electronic properties of layered materials can be modified greatly by chemical intercalation [44–46]. For example, Kim et al. intercalated a ferric chloride $(FeCl_3)_n$ inside the bilayer graphene and measured carrier density changes, suggesting chemical doping by the intercalant [85]. Two separate carrier densities were identified, which were associated with the intercalated and unintercalated domains in the bilayer graphene. For Bi_2Se_3 nanoplates intercalated

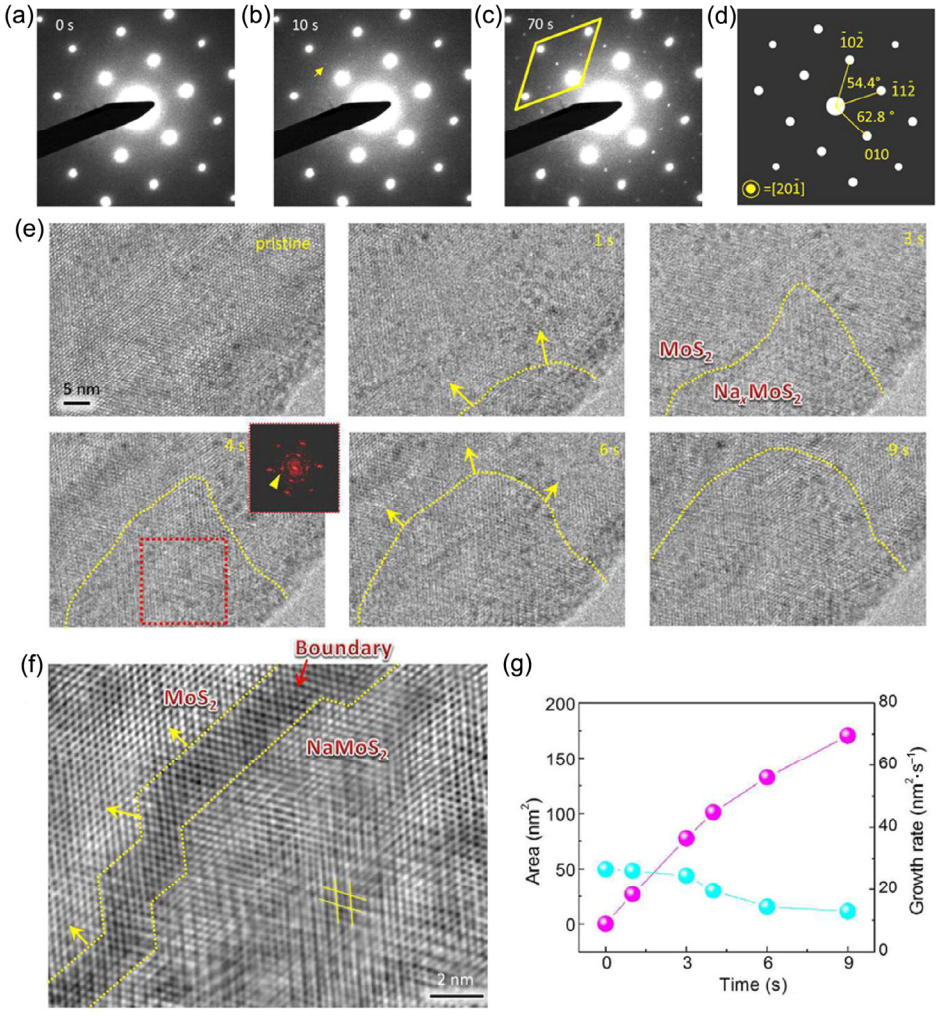

Figure 3 Phase transition in the MoS_2 nanosheet during Na^+ intercalation monitored by SAED patterns. (a) Pristine sample indexed to the 2H phase, (b) superlattice diffraction spots start to appear upon 10 s of Na^+ intercalation, and (c) the intensity of the superlattice spots increases after 70 s. (d) Simulated electron diffraction pattern of the 2H-MoS_2 matching the experimental pattern. Na^+-intercalated area evolution in the MoS_2 nanosheet characterized by HRTEM images: (e) time-resolved intercalation propagation. (f) Phase boundary between the intercalated and pristine regions, and (g) area and phase evolution growth rates. Reproduced with permission from Ref. [49], © American Chemical Society 2015.

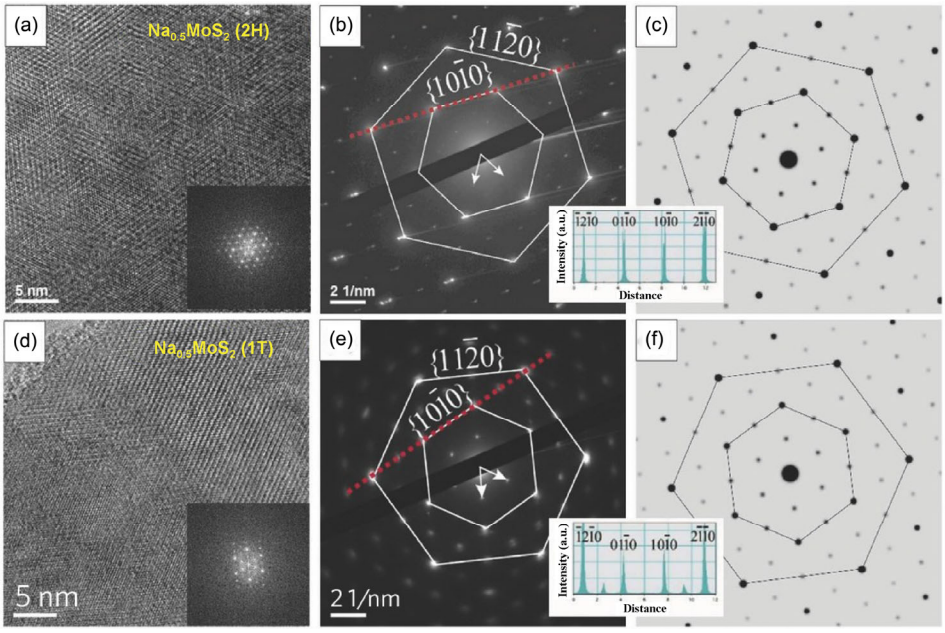

Figure 4 HRTEM image, FFT inset, captured and simulated SAED patterns of two regions after Na^+ intercalation in MoS_2: attributed to the 2H $Na_{0.5}MoS_2$ (a)–(c), and assigned to 1T $Na_{0.5}MoS_2$ (d)–(f). Note the intensity profile of the spots in the 2H phase (inset in (b)), compared to that of the spots in the 1T phase (inset in (e)). Reprinted with permission from Ref. [50], © John Wiley and Sons 2017.

with high density of zero-valent copper metal atoms [17], optical transmission was enhanced while the sheet resistance decreased by two to five times after intercalation. Even though the chemical intercalations have shown to modulate the properties of 2D materials greatly, they do not provide precise control over the concentration level and dynamics of intercalants into the hosting material, while often involving high processing temperatures and reactive reagents [45, 46, 54]. On the other hand, electrochemical intercalation can be more precisely and reversibly controlled.

The electrochemical intercalation typically relies on a battery-type configuration where an external bias is applied to electrochemically intercalate ions into the 2D materials through an ionically conducting solid or liquid electrolyte. The applied electrochemical voltage controls the dynamics and concentration of intercalating ions, thus manipulating the structure and properties of the 2D material host. Using standard electrochemistry techniques such as cyclic voltammetry, however, measuring sub-picoampere electrochemical currents produced from atomically thin 2D materials is difficult [54]. An electrochemical intercalation platform based on a planar nanobattery architecture has recently been developed to study the intercalation kinetics *in situ* through simultaneous structural and material property measurements during electrochemical intercalation [18, 32, 48, 53–55]. This section reviews several studies of *in situ* intercalation processes using the planar nanobattery platforms.

4.1 Li^+ intercalation in graphite nanosheets

Bao et al. used the planar nanobattery device to study the Li^+ intercalation kinetics in ultrathin graphite (3–60 graphene layers) [18]. The nanobattery device allows a real time correlation between the intercalation stage and optical transmittance spectra and electrical transport properties as a function of intercalation. As shown in Figs. 5(a)–5(c), a few-layer graphene sheet was placed on the pre-patterned copper electrodes on a glass substrate. Inside an Ar-filled glove box, a Li pellet was placed on an insulated electrical contact, followed by the addition of a liquid electrolyte (1 M $LiPF_6$ in w/w = 1/1 ethylene carbonate/diethyl carbonate), which covered both the ultrathin graphite and Li pellet. The whole device was then covered with a thin glass and sealed by polydimethylsiloxane (PDMS). The *in situ* optoelectronic measurements performed on the device revealed a reversible change in transmittance in the visible range at different stages of Li^+ intercalation (Fig. 5(d)). The changes in optical transmittance was attributed to the Fermi energy shift induced by electron doping by the intercalated Li ions, which modulates the inter-band transition and intra-band (Drude) optical conductivity. To distinguish different stages of intercalation, Raman spectra were taken before, during, and after Li^+ intercalation, which showed disappearance of the G peak of pristine graphene at 1,580 cm^{-1} upon full lithiation and formation of LiC_6 (Fig. 5(e)). *In situ* electrical transport measurements also showed lower sheet resistance in the intercalated state compared to the pristine state (Fig. 5(f)). A sheet conductivity of ~ 11 mS per layer was observed in the fully intercalated LiC_6 state. Additionally, room temperature Hall measurements showed electron carrier densities ranging from 3×10^{21} to 7×10^{21} cm^{-3} for LiC_{12} and from 1.5×10^{22} to 3.5×10^{22} cm^{-3} for LiC_6. Temperature dependent sheet resistance exhibited a transition behavior from weakly non-metallic in the pristine state to metallic in the LiC_6 state.

4.2 Li^+ intercalation in bilayer graphene using polymer electrolyte

The planar nanobattery platform [18, 32, 48] typically uses a liquid electrolyte for electrochemical intercalation, which could introduce additional experimental factors, such as charge impurities and strain fluctuations [53, 86–89]. Kuhne et al. used a solidified polymer electrolyte that partially covered a bilayer graphene [53]. This forces the Li^+ intercalation to be localized at one end of the device with most of the bilayer graphene free of the electrolyte (Fig. 6(a)). *In situ* Hall measurements across spatially displaced Hall probes were carried out to measure the in-plane Li diffusion kinetics. Assuming a complete charge transfer from Li^+ to the bilayer graphene, the density of intercalated Li ions, n_{Li}, follows $n_{Li}(x,t) = n(x,t) - n_{imp}(x,t=0)$, where n and n_{imp} are the charge carrier density and initial charge density from intrinsic doping sources of the bilayer. The extracted n_{Li} shows reversibility during repeated lithiation and delithiation cycles (Fig. 6(b)). The maximum carrier density is less than the electron density of C_6LiC_6 ($n \approx 6.36 \times 10^{14}$ cm^{-2}), thus the charge transfer ratio from Li^+ is less than one. The Li diffusion coefficient is extracted to be

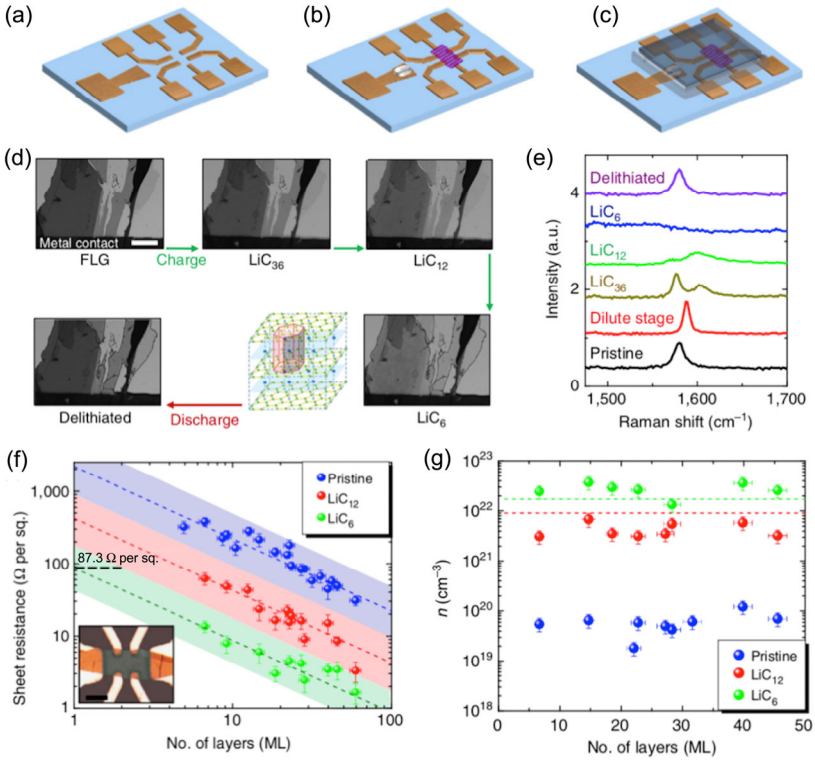

Figure 5 *In situ* investigation of Li^+ intercalation in graphite nanosheet using a planar nanobattery. (a)–(c) Schematics of the device fabrication process for *in situ* optical and electrical transport measurements. (d) Transmission optical microscope images and (e) Raman spectra of graphite sheets at different stages of Li^+ intercalation. (f) Sheet resistance and (g) carrier density versus thickness of graphite sheet at different lithiation stages [18]. Reproduced with permission from Ref. [18], © Nature Publication Group 2014.

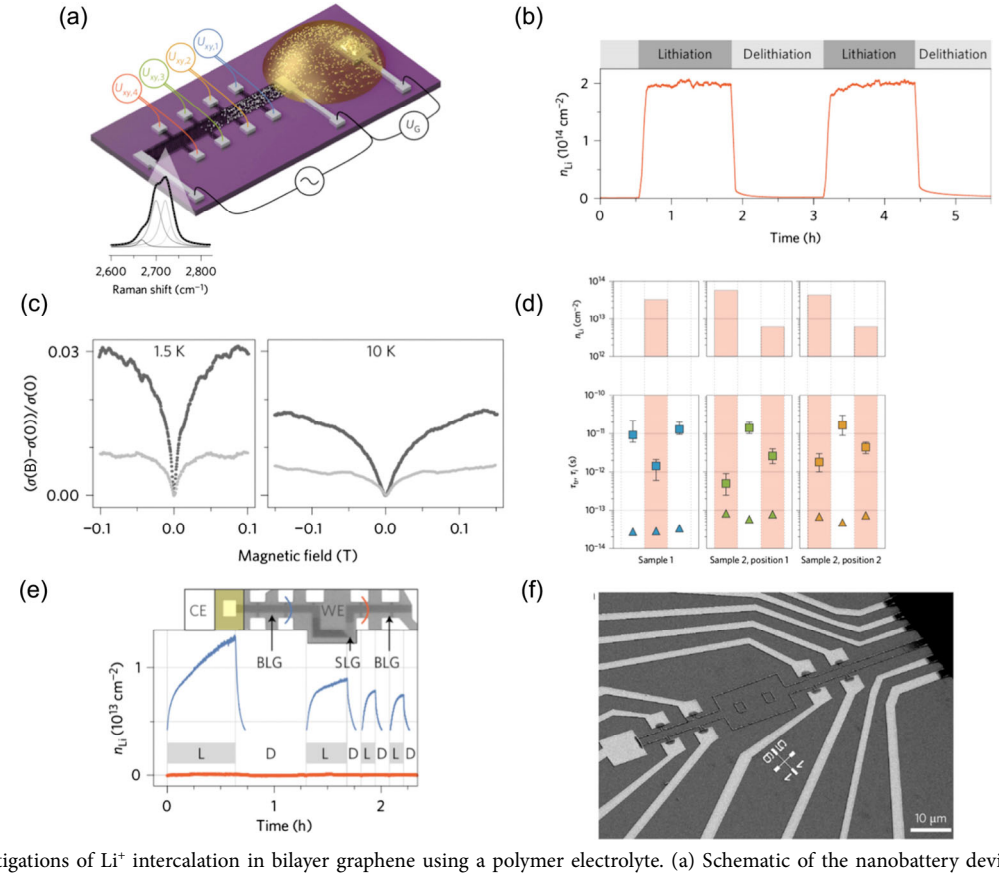

Figure 6 *In situ* investigations of Li^+ intercalation in bilayer graphene using a polymer electrolyte. (a) Schematic of the nanobattery device. The inset depicts the characteristic four-component Raman scattering response of bilayer graphene (an excitation wavelength of 488 nm). (b) Reversible change in the the concentration of intercalated Li ions upon lithiation/delithiation, extracted from Hall measurements at room temperature. (c) Magnetoconductivity traces in lithiated (dark grey) and delithiated (bright grey) state at 1.5 and 10 K. (d) Intervalley scattering time τ_i (squares) and transport time τ_{tr} (triangles) in pristine (white columns) and lithiated (orange columns) states. (e) Li^+ concentration n_{Li} versus time during lithiation (L)/delithiation (D) of a bilayer device (BLG) before and after a single layer graphene (SLG) junction. The Hall probe pairs are marked with the same color as the corresponding data set. (f) Scanning electron micrograph of a bilayer graphene device with two etched holes (~ 6 μm^2) after prolonged lithiation. Reproduced with permission from Ref. [53], © Nature Publication Group 2017.

as high as 7×10^{-5} $cm^2 \cdot s^{-1}$ by fitting the transient and one-dimensional Fick's second law for $n_{Li}(x,t)$ to the measured time-dependent charge densities at spatially displaced Hall probes.

The intercalated Li ions also induced inter-valley scattering in graphene, which was detected by monitoring the weak localization, a quantum correction to electron conductivity in the presence of a magnetic field due to electron scattering. Figure 6(c) shows an enhanced weak localization in the lithiated state compared to the delithiated state, from which the intervalley scattering time (τ_i) was extracted. Figure 6(d) shows a reduction in the intervalley scattering time (squares) during lithiation state (orange columns), indicating that Li ions increase the intervalley scattering rate of charge carriers in graphene bilayer. Finally, the Li ions were found to only diffuse in between the graphene sheets, and not between the graphene/SiO_2 or graphene/vacuum interfaces. This conclusion was based on comparing electrical properties of bilayer and single-layer graphene regions, which showed that a single layer graphene junction impeded the Li^+ diffusion (Fig. 6(e)). Li-rich edge decoration was observed at the inner edges of the macroscopic holes etched within the bilayer, caused by immobilized reaction products of the Li intercalate with impurities (Fig. 6(f)).

4.3 Li^+ intercalation in MoS_2 nanosheets

Using the same nanobattery platform, Wan et al. and Xiong et al. studied the lithiation dynamics and associated optical and electrical property changes in MoS_2 [32, 48]. As a time-trace, Wan et al. simultaneously measured electrochemical potential and the four-probe electrical resistance of a MoS_2 flake at a constant lithiation current of 0.5 μA (Fig. 7(a)). During the initial lithiation stage (region I), a rapid decrease of the electrochemical potential and a rapid decrease of the resistance were observed, which was attributed to Li^+ intercalation into 2H-MoS_2 with little lattice distortion. With increasing concentration of Li^+, region II appeared with an electrochemical potential plateau of ~ 1.1 V and lower resistance due to the formation of the metallic 1T-Li_xMoS_2 phase. At the onset of region III, a sharp rise in the resistance and another potential plateau of ~ 0.6 V were observed, corresponding to the irreversible conversion of 1T-$LiMoS_2$ to an insulating matrix composed of Li_2S and Mo nanoparticles. Interestingly, upon a rapid insertion of Li ions into MoS_2 (within a few minutes), a drastic decrease in resistance was observed from 5×10^5 to 190 ohms (Fig. 7(b)), which was attributed to the formation of a percolating metallic network of Mo nanoparticles. The thickness dependent relationship on the final resistance of the Li^+-intercalated MoS_2 is shown in Fig. 7(c).

Xiong et al. studied a reversible tuning of physical properties of MoS_2 films by varying the Li^+ concentration and measuring Raman spectra [48]. Figures 8(a)–8(h) shows a series of optical images of the MoS_2 flake at different cycles of Li intercalation. To prevent the irreversible conversion to Li_2S, the MoS_2 potential with respect to Li/Li^+ was kept above 1.1 V. Li^+ intercalation can be inferred from the changes in the optical transmission. Raman spectra show clearly the reversible phase transformation from the 2H to 1T phase with Li^+ intercalation and deintercalation (Fig. 8(i)). The enhanced optical transmission in the 1T phase could be understood from the intercalation-induced Fermi level shift as well as band structure change (schematic in Fig. 8(j)) [55]. After complete delithiation (Fig. 8(d)), the flake did not recover its initial color fully with the upper part of the flake being slightly reddish. This was attributed to intercalation-induced strain and increase in the MoS_2 interlayer spacing, which would accumulate upon repeated cycling with more red "bruises" (Figs. 8(f) and 8(h)). The observed E^1_{2g} peak broadening in Raman spectra is typically a sign of strain build-up and structural defects due to volume expansion in the MoS_2. Finally, the sheet resistance of the MoS_2 was tracked as a function of both thickness and the electrochemical potential (Figs. 8(k) and 8(l)), which showed orders of magnitude modulation in the sheet resistance, thus the carrier density.

4.4 Li^+ intercalation in vdW heterostructures

VdW heterostructures, constructed by stacking different atomic layers of 2D crystals, are novel functional materials with many design-specific exotic properties. Intercalation into the vdW heterointerfaces presents a rich playground for fundamental discoveries. Recently, Zhao et al. studied the electrochemical intercalation of Li ions into a vdW heterostructure of a single and bilayer graphene sandwiched between hexagonal boron nitride (h-BN) [54]. The electrochemical device was fabricated by a dry transfer technique [90] and shaped into a Hall bar geometry, with only the graphene edges in the vdW stack exposed to the electrolyte (Fig. 9(a)). The graphene layer was edge-contacted to a gold contact as the working electrode [90]. The gold contacts were covered with an electrochemically inert and electrically insulating SU-8 layer to prevent unwanted electrochemical side reactions. The device also used a solid electrolyte that covered the whole device. To probe the intercalation dynamics, magnetoresistance, optical spectroscopy, and low temperature quantum magneto-oscillation measurements were performed, *in situ*. At the early stage of intercalation, a linear increase in the electron density and corresponding decrease in the sheet resistance were observed in the graphene channel (Fig. 9(b)) due to the electrostatic gating through the h-BN dielectric. At the threshold voltage (~ 1.4 V for cycle 1), a rapid surge in the electron density accompanied with a spike in the sheet resistance was observed (Fig. 9(b)), which was attributed to the decrease in the electron mobility, consistent with increased intervalley scattering rate in the lithiated graphene layer. The resistance eventually decreases as the continued increase in carrier densities overcomes the decreased mobility. The threshold voltage changes with cycle number due to residual Li ions that do not fully de-intercalate. The evolution of Raman G and 2D peaks of graphene was tracked as a function of the electrochemical potential (Figs. 9(c) and 9(d)). The h-BN Raman peak appears unaffected

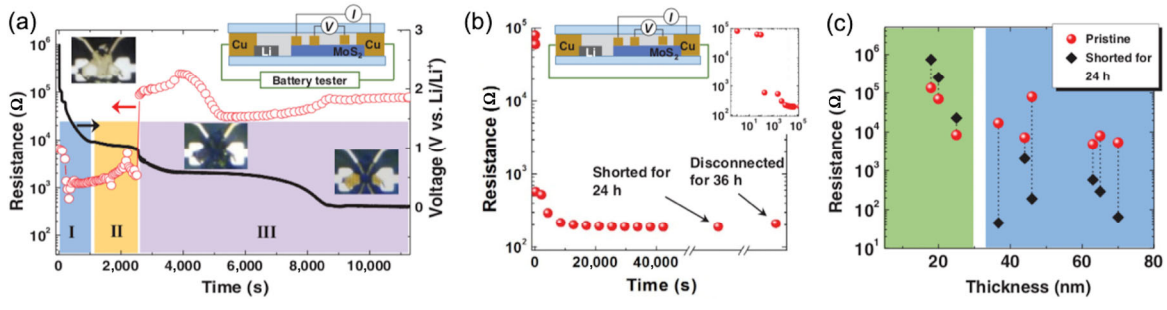

Figure 7 *In situ* investigation of Li^+ intercalation in MoS_2 nanosheet using a planar nanobattery. (a) Four-probe sheet resistance versus time of MoS_2 undergoing electrochemical lithiation at constant current. Insets show a schematic of the nanobattery for *in situ* resistance measurements (upper right), and optical images of the lithiated MoS_2 at stages I, II, and III, from left to right. (b) Resistance versus time for a MoS_2 sheet after electrically shorting the nanobattery. (c) Resistance versus thickness of the shorted MoS_2 sheets. Reproduced with permission from Ref. [32], © John Wiley and Sons 2015.

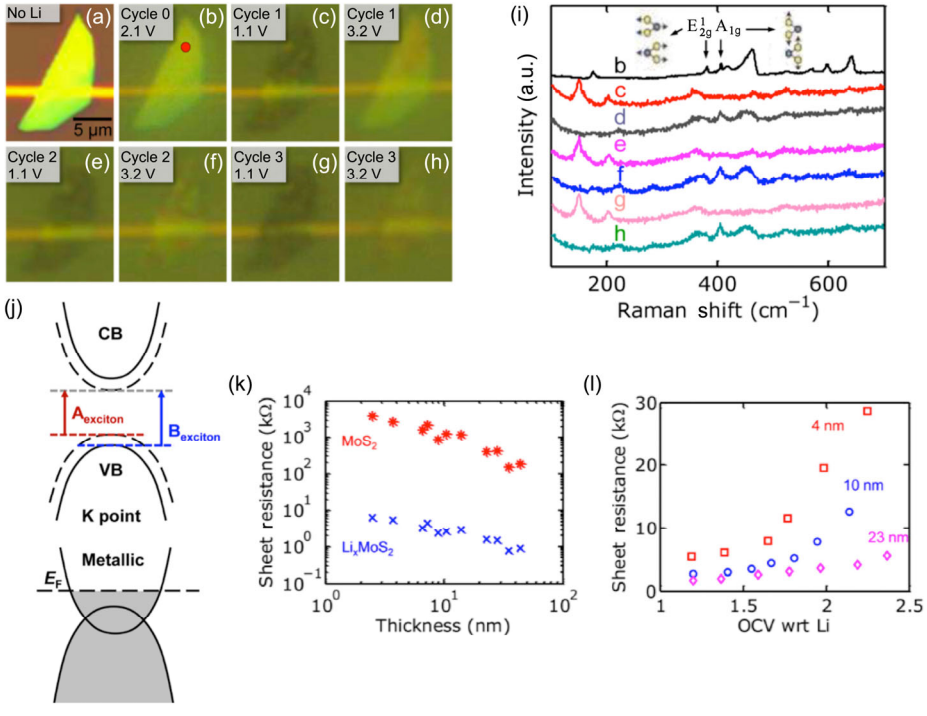

Figure 8 *In situ* investigations of Li^+ intercalation in MoS_2 nanosheet. (a)–(h) Optical reflection images of the MoS_2 sheet at different cycles of Li intercalations. (i) Raman spectra of the MoS_2 sheet at different cycles as indicated in the optical reflection images. (j) Schematics of the band structure of semiconducting 2H-MoS_2 (top) and metallic1T-Li_xMoS_2 (bottom) at the K-point in the Brillouin zone. Optical transitions due to the A and B excitons are shown. (k) Sheet resistance of the pristine and lithiated MoS_2 flakes of varying thicknesses. (l) Sheet resistance of Li_xMoS_2 flakes of different thicknesses, as a function of the electrochemical potentials vs. Li/Li^+. Reproduced with permission from Ref. [48], © American Chemical Society 2014.

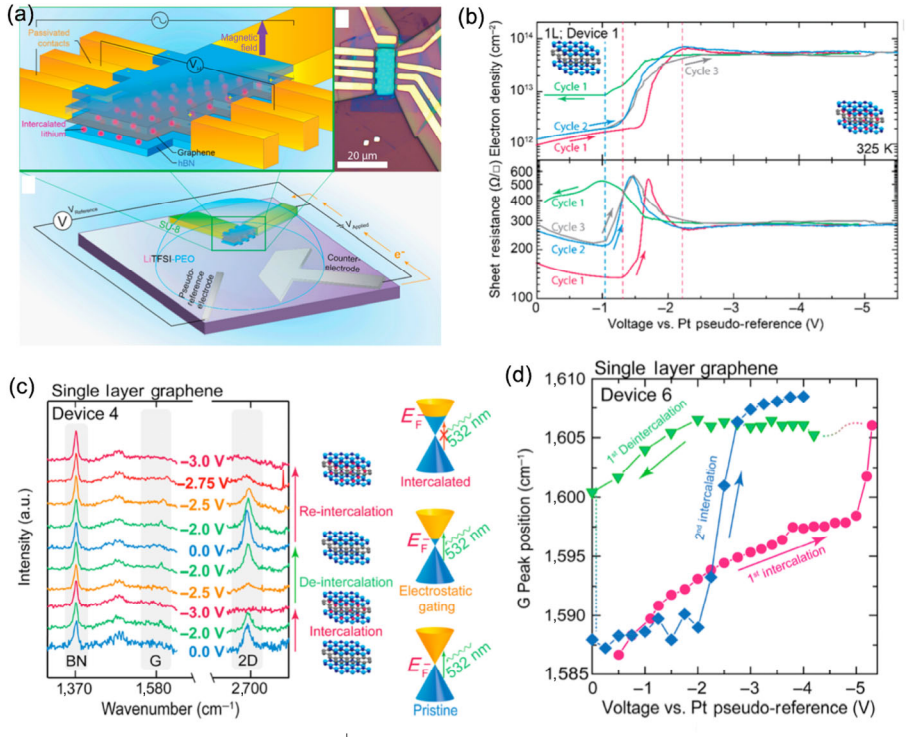

Figure 9 *In situ* investigations of Li^+ intercalation in graphene/hBN interfaces. (a) Schematic of the nanobattery device. The electrochemical reaction starts when a voltage is applied between the counter and the working electrode. The intercalation voltage is measured versus a Pt pseudo-reference. The Hall voltage is used to monitor the intercalation reaction. (b) The carrier density and sheet resistance as a function of the electrochemical potential. (c) Raman spectra evolution of single layer graphene during Li^+ intercalation and de-intercalation. Schematics of the Dirac cone shows the doping of the graphene and resulting Pauli blocking. (d) Changes in the graphene G peak position as a function of applied voltage. The sudden change in the G peak position shows the onset of intercalation stage at the threshold voltage. Reproduced with permission from Ref. [54], © American Chemical Society 2017.

by the intercalation while the G peak of the graphene blue shifts upon lithiation, and both G and 2D peaks disappear at high Li^+ concentrations. The low-temperature magnetotransport measurements on the single and bilayer graphene at a specific electrochemical potential reveal the electron density of 4.8×10^{14} and 7×10^{13} cm^{-2} for graphene/graphene and graphene/h-BN interfaces, respectively,

indicating the interface between two graphene sheets is far more amenable to hosting Li ions.

In a very recent work, Bediako et al. employed the same electrochemical device platform to study the role of the different vdW heterointerfaces on Li^+ electrochemical intercalation behavior of 2D heterostructures stacked by h-BN, graphene, and molybdenum dichalcogenide (MoX_2; X = S, Se) with various arrangements [55]. *In situ* photoluminescence reveals that a strongly electron-doped 1H-MoS_2 phase persists up to the onset of main Li^+ intercalation stage at electrochemical voltage of ~ 3 V, beyond which the negatively charged trions (A^-) start to appear and the photoluminescence is eventually quenched (Fig. 10(a)). This is consistent with the vanishing of the Raman spectral features of MoS_2 layer due to Pauli blocking upon full lithiation. With delithiation, the original Raman signatures of graphene are recovered, while the spectral intensity of the A_{1g} and E^1_{2g} modes of MoS_2 is reduced accompanied with the appearance of *J* modes around 150 and 230 cm^{-1} corresponding to the metallic T phase and an additional lattice distortion denoted as T′ phase (Fig. 10(b)). The magnetotransport studies at low temperature show a weak localization behavior as manifested by a pronounced peak near $B = 0$ due to enhanced intervalley scattering of intercalated Li ions (Fig. 10(c)). Comparison of carrier densities extracted from Hall measurements and the Shubnikov-de Hass oscillations (Fig. 10(c)) indicate that there are two conducting channels for the graphene/TMDC heterostructure: one is a high-mobility channel in the graphene layer with the electron density of 2×10^{13} cm^{-2} and the other is in the TMDC layer with the carrier density of 3×10^{14} cm^{-2}. Surprisingly, the graphene/MoX_2 heterointerface is found to accumulate more than tenfold greater charge compared to the MoX_2/MoX_2 homointerface. Figure 10(d) schematically shows the proposed Li^+ intercalation mechanism in the vdW heterostructure, starting with the charge transfer to both graphene and MoX_2 layers due to electrostatic doping through the h-BN dielectric in the initial stages of the electrochemical intercalation, to eventually formation of a highly doped and nanocrystalline T′-MoX_2 upon complete intercalation.

5 Prospects of *in situ* TEM investigations of intercalation in TMDCs

5.1 VdW gap expansion due to intercalation

Monitoring the change in the lattice constant *c* perpendicular to the basal plane during intercalation can be quite interesting. For instance, in the case of Li^+, the ion radius (0.6 Å) is close to that of the interstitial octahedral hole (~ 0.7Å) [42]. Therefore, one can expect that the octahedral hole can readily accommodate Li^+ with slight expansion from Coulombic repulsions. Beside the enlargement to accommodate the intercalants in the gap, there is another contributor to the gap expansion or contraction, which comes from the change in the structure induced by charge transfer into the d band of the host material [42]. The lattice constant *c* expansion of 0.49 ± 0.03 Å has been measured in Li^+ intercalation in group 4 and 5 TMDCs, which is greater than the expansion by Li^+ insertion in graphite (0.36 Å), assuming the octahedral hole can at least provide the same amount of space for the intercalant as in graphite [42]. Wang et al. [47] reported *c* expansion from 12.3 to 14 Å upon Li^+ intercalation in MoS_2. Enyashin and Seifert [91] calculated the lattice constant *c* for 2H, 1T and 2T phase of Li_xMoS_2 as a function of *x*, increasing from 0.5 to 1. Their results predicted that the interlayer distance can be increased by 1–1.2 Å for all cases compared to the pure phases [91]. Due to the larger radius of Na ions (1.16 Å), larger gap expansions can be expected compared to Li^+ intercalations [61]. However, the SAED patterns obtained by Gao and Liu et al. [49] reported only a slight increase by ~ 1.0%. The authors attributed this subtle gap expansion to crack formations and relaxation of the induced strain in the lattice. The mechanism and distribution of this crack formation is unclear and requires further investigations. Somoano et al. [92] reported interlayer distance change, Δd, of 3.37, 1.35, 2.14, 2.45, and 3.66 Å for solution-intercalated Li_xMoS_2 (2H) ($0.4 < x < 1$), Na_xMoS_2 (2H) ($0.3 < x < 0.6$), $K_{0.4}MoS_2$ (2H), $Rb_{0.3}MoS_2$ (2H), and $Cs_{0.3}MoS_2$ (2H) [92], respectively.

5.2 Kinetics of intercalations: From monovalent to organic intercalants

An *in situ* dynamic observation of various intercalant diffusions can be very compelling. For instance, the ionic radius of Mg^{2+} (0.72 Å) is slightly smaller than that of Li^+, thus the effects of stronger Coulombic interactions on the kinetics of intercalation and structural evolution can be investigated using Mg^{2+}. Mg^{2+} (divalent) intercalation in TMDCs, such as TiS_2, VS_2, and ZrS_2, has been achieved through chemical methods for battery applications [93, 94] albeit limited concentrations compared to the monovalent alkali metals. Studying the dynamics of the zero-valent intercalation in TMDCs is also appealing as it can enlighten vdW gap size change without the contribution from electron transfer and Coulombic repulsion or

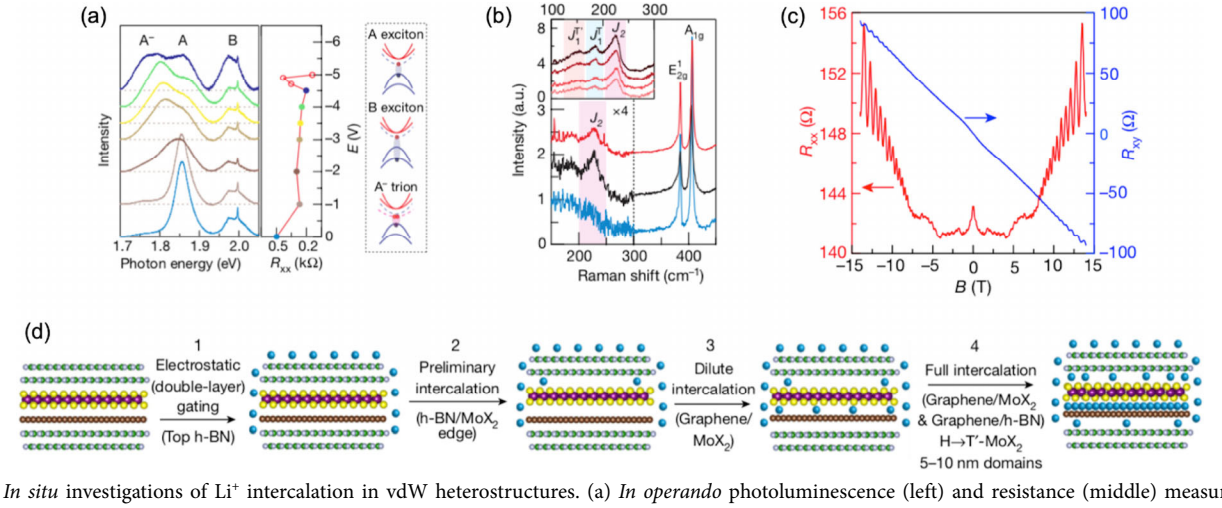

Figure 10 *In situ* investigations of Li^+ intercalation in vdW heterostructures. (a) *In operando* photoluminescence (left) and resistance (middle) measurements for graphene/MoS_2 at 325 K. The schematic on the right shows the exciton quasiparticles. (b) *Ex situ* Raman spectra of a pristine (bottom), cycled (middle) and annealed (top) heterostructure. Inset, Raman spectra after annealing of MoS_2, graphene/MoS_2, 2L-MoS_2, and graphene/2L-MoS_2 (from bottom to top). (c) Four-terminal R_{xx} and R_{xy} as a function of magnetic field. (d) Proposed intercalation mechanism of the vdW heterostructure. Reproduced with permission from Ref. [55], © Nature Publication Group 2018.

attraction. Methods to intercalate zero-valent metals, such as Ag, Au, Co, Cu, Fe, In, Ni, and Sn [46, 56, 95] have been developed for layered materials. In the case of Cu^0 intercalation, 60 atomic percent intercalation was obtained in Bi_2Se_3. The charge neutrality of these intercalants was confirmed by X-ray photoelectron spectroscopy (XPS) and electron energy-loss spectroscopy (EELS) [95].

The dynamics of different intercalants in various layered materials, other than Li^+ in graphene, have not been yet characterized. It is interesting to understand how different intercalant species diffuse in various layered material systems, phases and stacking orders. Thus, it is essential to develop devices that allow intercalation while keeping the sample areas of interest undisturbed from the electrolyte for close examination. In addition, developing various hetero vdW gaps provide a window of opportunities for better understanding of the diffusion mechanisms. For instance, intercalation kinetics in h-BN-MoS_2, graphene-MoS_2, MoS_2-MoS_2 or MoS_2-$MoSe_2$ hetero-structures is appealing for investigation, with energy implications in batteries and a subset of pseudocapacitors. Another under-explored area that requires further attention is the diffusion characteristics of magnetic intercalants, and an inquiry into possible magnetic or paramagnetic spin ordering formations.

5.3 Evolution of superstructures in intercalated TMDCs

Superlattice complexes can be formed by ordering of the intercalants at certain concentrations or induced by charge density waves (CDWs) instabilities. CDWs are electronic density fluctuations with periodicity; under certain conditions, the CDWs can displace atoms from their higher symmetries [42, 96]. A gap is opened at the reciprocal lattice (at $2\boldsymbol{k}_F$, where $\boldsymbol{k}_F$ denotes the Fermi wave vector), which can drive a superlattice transition [42]. This is accompanied by dramatic changes in the density of states at the Fermi level influencing the transport properties [42]. On the other hand, superlattice transitions induced by ordering of the intercalants is a thermodynamic phenomenon of electrostatic interactions with no gap opening in the reciprocal lattice. Investigating the dynamics of the superlattice formations in the intercalated systems such as TiS_2 and TaS_2 can be quite fruitful for a better understanding of their formations and evolutions. One appealing research topic is to understand the effects of intercalations on the formation or suppression of CDWs. Intercalation has been used for suppression of CDWs and emergence of superconductivity [97, 98] such as Cu intercalation in 1T-$TiSe_2$ [9, 99] or Na^+ in $NbSe_2$ [100]. Combining TEM and transport investigation of these superlattice complexes will lead to a better understanding of their formation and effects on the material properties.

5.4 Atomic resolution imaging of intercalants along *a* or *b* directions

While the small size of Li^+ hinders its direct imaging in the gap, atomic scale resolution of Na^+ intercalation in interlayers of MoS_2 was reported by Wang et al. [101] (Fig. 11). Na ions were intercalated in to MoS_2 using a battery cell, outside TEM. The *in situ* and *ex situ* XRD results of their cells showed structural changes of MoS_2 as the voltage approached below 1 V. A phase transition from 2H MoS_2 ($2\theta_{(002)}$ = 14.38, a = 3.16 Å and c = 12.29 Å) to 2H $Na_{0.5}MoS_2$ ($2\theta_{(002)}$ = 11.82, a = 3.21 Å and c = 15.06 Å) was detected around 0.85 V, and from 2H $Na_{0.5}MoS_2$ to 1T $NaMoS_2$ ($2\theta_{(002)}$ = 12.42, a = 3.11 Å and c = 14.29 Å) at 0.75 V. Further intercalation below 0.75V induced a decomposition phase corresponding to Na_xS ($2\theta_{(002)}$ = 12.80, a = 3.43 Å and c = 13.91 Å). Atomic scale imaging of the structure was obtained by aberration-corrected scanning transmission electron microscopy (STEM) (Figs. 11(i)–11(l)). The analysis revealed that Na ions initially occupy every other interlayer until forming the hexagonal $Na_{0.5}MoS_2$, while the other interlayers remained unfilled. After the 2H to 1T phase transition, and upon further intercalation, all the remaining empty interlayers were filled forming $2a \times 2a$ structures (Figs. 11(h) and 11(l)). The average gap spacing was increased from the initial value of 0.61–0.68 to 0.72 nm by Na^+ insertion. Further intercalation decomposed the MoS_2 into the metallic Mo and hexagonal Na_xS, at which point the recovery of the

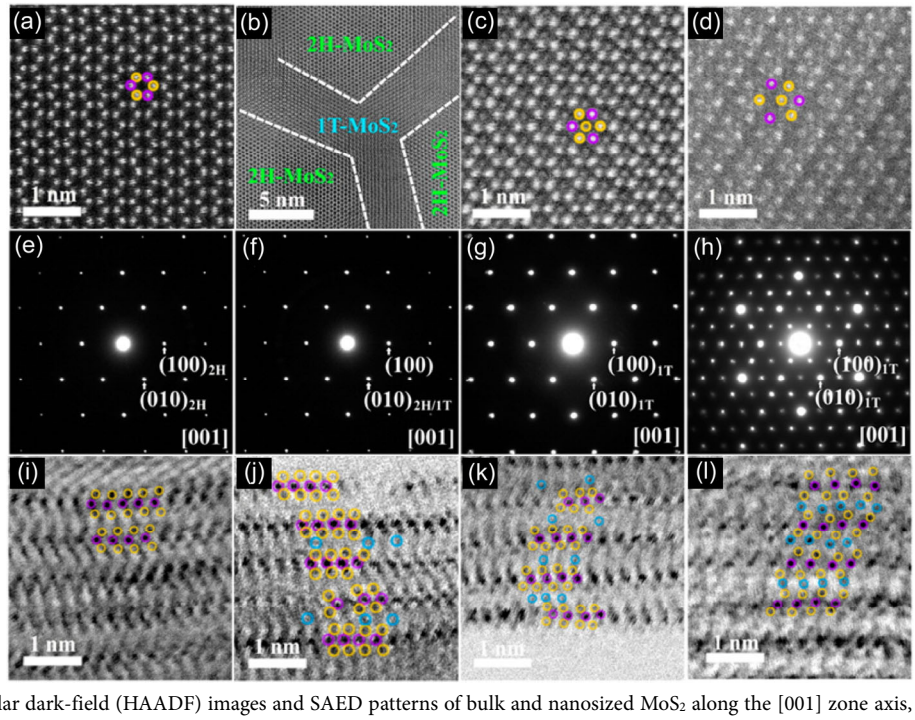

Figure 11 High-angle annular dark-field (HAADF) images and SAED patterns of bulk and nanosized MoS_2 along the [001] zone axis, intercalated with Na^+ inside a battery cell at specific capacities of 60 ((a) and (e)), 80 ((b) and (f)), 160 ((c) and (g)), and 256 mAh·g^{-1} ((d) and (h)). According to the SAED patterns, Na^+ intercalation involved transition from 2H ((a) and (e)) to 1T ((c) and (g)) with a $2a \times 2a$ superstructure ((d) and (h)). Note that the Na ions first intercalate in every other interlayer, and with further intercalation fill the empty gaps. Annular bright-field (ABF) images of as-prepared nano-MoS_2 along the [100] zone axis (i), and discharged at 1.0 V (j), 0.8 V (k), and 0.2 V (l). The purple, yellow, and blue circles represent Mo, S, and Na atoms, respectively. Reprinted with permission from Ref. [101], © American Chemical Society 2014.

structure was not possible. After the decomposition, no Mo clusters were observed by STEM until very low potentials (0.01 V) indicating that the metallic Mo phase was well-dispersed in the structure.

The information obtained from the study by Wang et al. [101] underscores the value of atomic-resolution TEM characterizations of intercalation in layered materials. An alluring target is to design an experiment to capture dynamics of intercalations in TMDCs at sub-Ångström resolutions. This can lead to a better understanding of the atomic interactions, thereby structural evolution in the interlayer gaps. The layer-dependent occupancy of Li^+ has also been observed and established for intercalation in graphite. Intercalation in graphite involves several stages: starting from random distribution of Li^+ at a dilute level; then ion diffusion to fill every four (stage-4, LiC_{36}), three (stage-3, LiC_{27}), two (stage-2, LiC_{12}), and one (stage-1, LiC_6) layer(s) [102, 103]. However, the mechanism for layer-dependent intercalation in TMDCs remains unclear and requires further investigations.

5.5 Intercalation in few-layered materials

Kinetics and structural evolution of few-layer TMDC systems have yet to be characterized in detail. Recently, using a nanodevice equipped with a polymer electrolyte that partially wetted the sample, formation of a dense Li structure in a bilayer graphene was investigated by Kühne, Smet and co-workers [52]. The *in situ* characterizations were performed using a spherical and chromatic aberration correction electron microscope at a low voltage (80 kV). Figure 12 shows the images of the sample before applying the voltage to the counter electrode as well as a series of time-resolved images. After 170 s, a second lattice (beside graphene) started to emerge. FFT patterns identified formation of three additional domains upon intercalation. Comparison between the FFT pattern of the pristine bilayer and that of the intercalated sample showed a close-pack multilayer crystallization of the Li atoms encapsulated between the graphene layers. EELS signals of this crystalline region

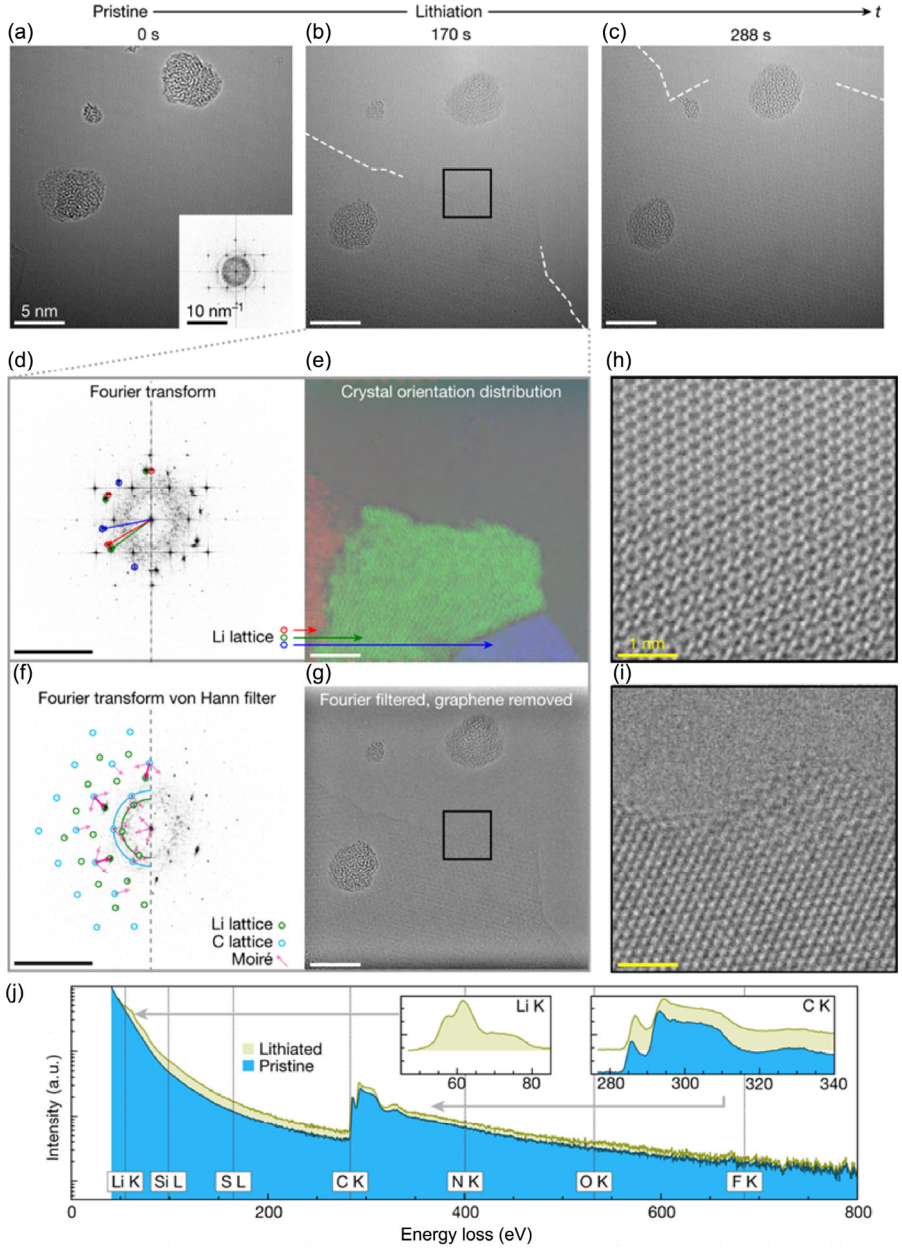

Figure 12 TEM characterizations of the dense Li crystal formed in the bilayer graphene: (a) pristine, before intercalation, (b) after 170 s, (c) after 288 s, (d) FFT pattern of panel (b). (e) Colored FFT maps showing three crystal domains of Li rotated relative to each other. (h) Magnified image of the box in panel (b). (f) von Hann-filtered Fourier transform of panel (b) showing the signals from Li and graphene lattices. (g) Fourier-filtered pattern of panel (b) with graphene lattice and moiré effects removed. (i) Magnified image of the box in panel (g). (j) EELS signals from before (blue) and during (yellow) lithiation. Reprinted with permission from Ref. [52], © Springer Nature 2018.

exhibited the Li K-edge at 55 eV. The experimental observations were further clarified by DFT calculations suggesting the plausibility of finite clusters and periodic hexagonal close-packed Li structure formations. The calculated energies were only 0.01–0.05 eV higher than that of the C_6LiC_6 per Li atom. The new findings by Kühne et al. [52] emphasized the need to re-examine the current understanding of intercalation, which is largely based on studies of bulk samples, in bilayer and few-layer systems. It showed that the confined nature of the atomically thin materials might exhibit effects, structures and, consequently, properties that can drastically be different from those of the bulk. Moreover, it is critical to control the intercalation precisely in these systems in order to acquire a detailed picture of the structural and electronic evolution. The UV-curable polymer electrolyte made it possible to contact only one side of the bilayer, leaving the rest of the material undisturbed for high resolution imaging. Evidently, such measurements are more challenging; however, they are essential for obtaining detailed knowledge of the intercalation. Given the variety of the intercalants and TMDC host materials, there is plenty of room for further investigation of intercalation in few-layered systems.

6 Summary and outlook

We provide a review of recent advances on the *in situ* structural and electronic property characterizations of intercalation in 2D layered materials and heterostructures, with the main focus on TMDCs. Planar nanobattery device platform has been effectively utilized to conduct multi-modal *in situ* characterizations. Structural changes induced by the intercalation dynamics have been characterized by the canvassed literature including diffusion rates of the reaction fronts, phase transformation and superlattice formations. Overall, current intercalation kinetic studies, while providing important information, will benefit from deeper investigations. A compelling area of research is to characterize the intercalation dynamics in bilayers, few layers and heterostructures, especially along *a* or *b* axis, at higher spatial resolution. In addition, the kinetics of other intercalants (other than Li^+ and Na^+) and other TMDC host materials have not been studied. Examining the hosting capability of various vdW gaps in homo/heterointerfaces for different intercalants can shed light on the scope of implementation of electrochemically controlled intercalation in tailoring material properties. A rational design for coupled and *in situ* electrical, optical, thermal, and structural characterizations of intercalation processes is critical to unveil the causal relationship between intercalation phenomena and property/structural changes. Given the fact that the electronic structure of TMDCs is greatly influenced by perturbation in its lattice atomic arrangement, it is fundamentally thought-provoking to investigate the role of quantifiable number of intrinsic and extrinsic structural defects in the kinetics of intercalation in terms of charge distribution and ion diffusion.

Acknowledgements

S. Y. is supported by the National Science Foundation Division of Chemical, Bioengineering, Environmental, and Transport Systems (No. 1749742). M. Y. is supported by the Department of Energy (DE-SC0014476). J. J. C. acknowledges support from the Army Research Office (No. 71816-MS).

References

[1] Li, X. L.; Wang, X. R.; Zhang, L.; Lee, S.; Dai, H. J. Chemically derived, ultrasmooth graphene nanoribbon semiconductors. *Science* **2008**, *319*, 1229–1232.

[2] Radisavljevic, B.; Radenovic, A.; Brivio, J.; Giacometti, V.; Kis, A. Single-layer MoS_2 transistors. *Nat. Nanotechnol.* **2011**, *6*, 147–150.

[3] Wilson, J. A.; Yoffe, A. D. The transition metal dichalcogenides discussion and interpretation of the observed optical, electrical and structural properties. *Adv. Phys.* **1969**, *18*, 193–335.

[4] Geim, A. K.; Grigorieva, I. V. Van der Waals heterostructures. *Nature* **2013**, *499*, 419–425.

[5] Wang, F.; Zhang, Y. B.; Tian, C. S.; Girit, C.; Zettl, A.; Crommie, M.; Shen, Y. R. Gate-variable optical transitions in graphene. *Science* **2008**, *320*, 206–209.

[6] Li, Z. Q.; Henriksen, E. A.; Jiang, Z.; Hao, Z.; Martin, M. C.; Kim, P.; Stormer, H. L.; Basov, D. N. Dirac charge dynamics in graphene by infrared spectroscopy. *Nat. Phys.* **2008**, *4*, 532–535.

[7] Feng, J.; Qian, X. F.; Huang, C. W.; Li, J. Strain-engineered artificial atom as a broad-spectrum solar energy funnel. *Nat. Photonics* **2012**, *6*, 866–872.

[8] Hor, Y. S.; Williams, A. J.; Checkelsky, J. G.; Roushan, P.; Seo, J.; Xu, Q.; Zandbergen, H. W.; Yazdani, A.; Ong, N. P.; Cava, R. J. Superconductivity in $Cu_xBi_2Se_3$ and its implications for pairing in the undoped topological insulator. *Phys. Rev. Lett.* **2010**, *104*, 057001.

[9] Morosan, E.; Zandbergen, H. W.; Dennis, B. S.; Bos, J. W. G.; Onose, Y.; Klimczuk, T.; Ramirez, A. P.; Ong, N. P.; Cava, R. J. Superconductivity in Cu_xTiSe_2. *Nat. Phys.* **2006**, *2*, 544–550.

[10] Profeta, G.; Calandra, M.; Mauri, F. Phonon-mediated superconductivity in graphene by lithium deposition. *Nat. Phys.* **2012**, *8*, 131–134.

[11] Zhang, R. Y.; Tsai, I. L.; Chapman, J.; Khestanova, E.; Waters, J.; Grigorieva, I. V. Superconductivity in potassium-doped metallic polymorphs of MoS_2. *Nano Lett.* **2016**, *16*, 629–636.

[12] Ye, J. T.; Zhang, Y. J.; Akashi, R.; Bahramy, M. S.; Arita, R.; Iwasa, Y. Superconducting dome in a gate-tuned band insulator. *Science* **2012**, *338*, 1193–1196.

[13] Morosan, E.; Zandbergen, H. W.; Li, L.; Lee, M.; Checkelsky, J. G.; Heinrich, M.; Siegrist, T.; Ong, N. P.; Cava, R. J. Sharp switching of the magnetization in $Fe_{1/4}TaS_2$. *Phys. Rev. B* **2007**, *75*, 104401.

[14] Hardy, W. J.; Chen, C. W.; Marcinkova, A.; Ji, H.; Sinova, J.; Natelson, D.; Morosan, E. Very large magnetoresistance in $Fe_{0.28}TaS_2$ single crystals. *Phys. Rev. B* **2015**, *91*, 054426.

[15] Koski, K. J.; Cha, J. J.; Reed, B. W.; Wessells, C. D.; Kong, D. S.; Cui, Y. High-density chemical intercalation of zero-valent copper into Bi_2Se_3 nanoribbons. *J. Am. Chem. Soc.* **2012**, *134*, 7584–7587.

[16] Cha, J. J.; Koski, K. J.; Huang, K. C. Y.; Wang, K. X.; Luo, W. D.; Kong, D. S.; Yu, Z. F.; Fan, S. H.; Brongersma, M. L.; Cui, Y. Two-dimensional chalcogenide nanoplates as tunable metamaterials via chemical intercalation. *Nano Lett.* **2013**, *13*, 5913–5918.

[17] Yao, J.; Koski, K. J.; Luo, W. D.; Cha, J. J.; Hu, L. B.; Kong, D. S.; Narasimhan, V. K.; Huo, K. F.; Cui, Y. Optical transmission enhacement through chemically tuned two-dimensional bismuth chalcogenide nanoplates. *Nat. Commun.* **2014**, *5*, 5670.

[18] Bao, W. Z.; Wan, J. Y.; Han, X. G.; Cai, X. H.; Zhu, H. L.; Kim, D.; Ma, D. K.; Xu, Y. L.; Munday, J. N.; Drew, H. D. et al. Approaching the limits of transparency and conductivity in graphitic materials through lithium intercalation. *Nat. Commun.* **2014**, *5*, 4224.

[19] Wang, Y. C.; Ou, J. Z.; Balendhran, S.; Chrimes, A. F.; Mortazavi, M.; Yao, D. D.; Field, M. R.; Latham, K.; Bansal, V.; Friend, J. R. et al. Electrochemical control of photoluminescence in two-dimensional MoS_2 nanoflakes. *ACS Nano* **2013**, *7*, 10083–10093.

[20] Wan, C. L.; Wang, Y. F.; Wang, N.; Norimatsu, W.; Kusunoki, M.; Koumoto, K. Intercalation: Building a natural superlattice for better thermoelectric performance in layered chalcogenides. *J. Electron. Mater.* **2011**, *40*, 1271–1280.

[21] Kang, J. S.; Ke, M.; Hu, Y. J. Ionic intercalation in two-dimensional van der Waals materials: *In situ* characterization and electrochemical control of the anisotropic thermal conductivity of black phosphorus. *Nano Lett.* **2017**, *17*, 1431–1438.

[22] Sood, A.; Xiong, F.; Chen, S. D.; Wang, H. T.; Selli, D.; Zhang, J. S.; McClellan, C. J.; Sun, J.; Donadio, D.; Cui, Y. et al. An electrochemical thermal transistor. *Nat. Commun.* **2018**, *9*, 4510.

[23] Coleman, J. N.; Lotya, M.; O'Neill, A.; Bergin, S. D.; King, P. J.; Khan, U.; Young, K.; Gaucher, A.; De, S.; Smith, R. J. et al. Two-dimensional nanosheets produced by liquid exfoliation of layered materials. *Science* **2011**, *331*, 568–571.

[24] Withers, F.; Yang, H.; Britnell, L.; Rooney, A. P.; Lewis, E.; Felten, A.; Woods, C. R.; Sanchez Romaguera, V.; Georgiou, T.; Eckmann, A. et al. Heterostructures produced from nanosheet-based inks. *Nano Lett.* **2014**, *14*, 3987–3992.

[25] Wang, H. T.; Lu, Z. Y.; Xu, S. C.; Kong, D. S.; Cha, J. J.; Zheng, G. Y.; Hsu, P. C.; Yan, K.; Bradshaw, D.; Prinz, F. B. et al. Electrochemical tuning of vertically aligned MoS_2 nanofilms and its application in improving hydrogen evolution reaction. *Proc. Natl. Acad. Sci. USA* **2013**, *110*, 19701–19706.

[26] Lukowski, M. A.; Daniel, A. S.; Meng, F.; Forticaux, A.; Li, L. S.; Jin, S. Enhanced hydrogen evolution catalysis from chemically exfoliated metallic MoS_2 nanosheets. *J. Am. Chem. Soc.* **2013**, *135*, 10274–10277.

[27] Voiry, D.; Salehi, M.; Silva, R.; Fujita, T.; Chen, M. W.; Asefa, T.; Shenoy, V. B.; Eda, G.; Chhowalla, M. Conducting MoS_2 nanosheets as catalysts for hydrogen evolution reaction. *Nano Lett.* **2013**, *13*, 6222–6227.

[28] Voiry, D.; Yamaguchi, H.; Li, J. W.; Silva, R.; Alves, D. C. B.; Fujita, T.; Chen, M. W.; Asefa, T.; Shenoy, V. B.; Eda, G. et al. Enhanced catalytic activity in strained chemically exfoliated WS_2 nanosheets for hydrogen evolution. *Nat. Mater.* **2013**, *12*, 850–855.

[29] Zhou, Y.; Silva, J. L.; Woods, J. M.; Pondick, J. V.; Feng, Q. L.; Liang, Z. X.; Liu, W.; Lin, L.; Deng, B. C.; Brena, B. et al. Revealing the contribution of individual factors to hydrogen evolution reaction catalytic activity. *Adv. Mater.* **2018**, *30*, 1706076.

[30] Acerce, M.; Voiry, D.; Chhowalla, M. Metallic 1T phase MoS_2 nanosheets as supercapacitor electrode materials. *Nat. Nanotechnol.* **2015**, *10*, 313–318.

[31] Zhu, Y.; Peng, L. L.; Fang, Z. W.; Yan, C. S.; Zhang, X.; Yu, G. H. Structural engineering of 2D nanomaterials for energy storage and catalysis. *Adv. Mater.* **2018**, *30*, 1706347.

[32] Wan, J. Y.; Bao, W. Z.; Liu, Y.; Dai, J. Q.; Shen, F.; Zhou, L. H.; Cai, X. H.; Urban, D.; Li, Y. Y.; Jungjohann, K. et al. *In situ* investigations of Li-MoS_2 with planar batteries. *Adv. Energy Mater.* **2015**, *5*, 1401742.

[33] Zhu, Y.; Qian, Y. M.; Ju, Z. Y.; Peng, L. L.; Yu, G. H. Solvent-dependent intercalation and molecular configurations in metallocene-layered crystal superlattices. *Nano Lett.* **2018**, *18*, 6071–6075.

[34] Chen, D. H.; Peng, L. L.; Yuan, Y. F.; Zhu, Y.; Fang, Z. W.; Yan, C. S.; Chen, G.; Shahbazian-Yassar, R.; Lu, J.; Amine, K. et al. Two-dimensional Holey Co_3O_4 nanosheets for high-rate alkali-ion batteries: From rational synthesis to *in situ* probing. *Nano Lett.* **2017**, *17*, 3907–3913.

[35] Xue, Y. H.; Zhang, Q.; Wang, W. J.; Cao, H.; Yang, Q. H.; Fu, L. Opening two-dimensional materials for energy conversion and storage: A concept. *Adv. Energy Mater.* **2017**, *7*, 1602684.

[36] Liang, Y. L.; Yoo, H. D.; Li, Y. F.; Shuai, J.; Calderon, H. A.; Robles Hernandez, F. C.; Grabow, L. C.; Yao, Y. Interlayer-expanded molybdenum disulfide nanocomposites for electrochemical magnesium storage. *Nano Lett.* **2015**, *15*, 2194–2202.

[37] Yarali, M.; Biçer, E.; Gürsel, S. A.; Yürüm, A. The effect of pH on the interlayer distances of elongated titanate nanotubes and their use as a Li-ion battery anode. *Nanotechnology* **2016**, *27*, 015401.

[38] Yarali, M.; Biçer, E.; Gürsel, S. A.; Yürüm, A. Expansion of titanate nanotubes by the use of a surfactant and its improved performance as an anode in Li-ion batteries. *Electrochim. Acta* **2016**, *220*, 453–464.

[39] Kashfi-Sadabad, R.; Yazdani, S.; Huan, T. D.; Cai, Z.; Pettes, M. T. Role of oxygen vacancy defects in the electrocatalytic activity of substoichiometric molybdenum oxide. *J. Phys. Chem. C* **2018**, *122*, 18212–18222.

[40] Yazdani, S.; Kashfi-Sadabad, R.; Huan, T. D.; Morales-Acosta, M. D.; Pettes, M. T. Polyelectrolyte-assisted oxygen vacancies: A new route to defect engineering in molybdenum oxide. *Langmuir* **2018**, *34*, 6296–6306.

[41] Yazdani, S.; Pettes, M. T. Nanoscale self-assembly of thermoelectric materials: A review of chemistry-based approaches. *Nanotechnology* **2018**, *29*, 432001.

[42] Dresselhaus, M. S. *Intercalation in Layered Materials*; Springer Science+ Business Media, LLC: New York, 1986.

[43] Chhowalla, M.; Shin, H. S.; Eda, G.; Li, L. J.; Loh, K. P.; Zhang, H. The chemistry of two-dimensional layered transition metal dichalcogenide nanosheets. *Nat. Chem.* **2013**, *5*, 263–275.

[44] Wang, H. T.; Yuan, H. T.; Sae Hong, S.; Li, Y. B.; Cui, Y. Physical and chemical tuning of two-dimensional transition metal dichalcogenides. *Chem. Soc. Rev.* **2015**, *44*, 2664–2680.

[45] Wan, J. Y.; Lacey, S. D.; Dai, J. Q.; Bao, W. Z.; Fuhrer, M. S.; Hu, L. B. Tuning two-dimensional nanomaterials by intercalation: Materials, properties and applications. *Chem. Soc. Rev.* **2016**, *45*, 6742–6765.

[46] Jung, Y.; Zhou, Y.; Cha, J. J. Intercalation in two-dimensional transition metal chalcogenides. *Inorg. Chem. Front.* **2016**, *3*, 452–463.

[47] Wang, L. F.; Xu, Z.; Wang, W. L.; Bai, X. D. Atomic mechanism of dynamic electrochemical lithiation processes of MoS_2 nanosheets. *J. Am. Chem. Soc.* **2014**, *136*, 6693–6697.

[48] Xiong, F.; Wang, H. T.; Liu, X. G.; Sun, J.; Brongersma, M.; Pop, E.; Cui, Y. Li intercalation in MoS_2: *In situ* observation of its dynamics and tuning optical and electrical properties. *Nano Lett.* **2015**, *15*, 6777–6784.

[49] Gao, P.; Wang, L. P.; Zhang, Y. Y.; Huang, Y.; Liu, K. H. Atomic-scale probing of the dynamics of sodium transport and intercalation-induced phase transformations in MoS_2. *ACS Nano* **2015**, *9*, 11296–11301.

[50] Huang, Q. M.; Li, X. M.; Sun, M. H.; Zhang, L.; Song, C. Z.; Zhu, L.; Chen, P.; Xu, Z.; Wang, W. L.; Bai, X. D. The mechanistic insights into the 2H-1T phase transition of MoS_2 upon alkali metal intercalation: From the study of dynamic sodiation processes of MoS_2 nanosheets. *Adv. Mater. Interfaces* **2017**, *4*, 1700171.

[51] Zhang, J. S.; Yang, A. K.; Wu, X.; van de Groep, J.; Tang, P. Z.; Li, S. R.; Liu, B. F.; Shi, F. F.; Wan, J. Y.; Li, Q. T. et al. Reversible and selective ion intercalation through the top surface of few-layer MoS_2. *Nat. Commun.* **2018**, *9*, 5289.

[52] Kühne, M.; Börrnert, F.; Fecher, S.; Ghorbani-Asl, M.; Biskupek, J.; Samuelis, D.; Krasheninnikov, A. V.; Kaiser, U.; Smet, J. H. Reversible superdense ordering of lithium between two graphene sheets. *Nature* **2018**, *564*, 234–239.

[53] Kühne, M.; Paolucci, F.; Popovic, J.; Ostrovsky, P. M.; Maier, J.; Smet, J. H. Ultrafast lithium diffusion in bilayer graphene. *Nat. Nanotechnol.* **2017**, *12*, 895–900.

[54] Zhao, S. Y. F.; Elbaz, G. A.; Bediako, D. K.; Yu, C.; Efetov, D. K.; Guo, Y. S.; Ravichandran, J.; Min, K. A.; Hong, S.; Taniguchi, T. et al. Controlled electrochemical intercalation of graphene/h-BN van der Waals heterostructures. *Nano Lett.* **2018**, *18*, 460–466.

[55] Bediako, D. K.; Rezaee, M.; Yoo, H.; Larson, D. T.; Zhao, S. Y. F.; Taniguchi, T.; Watanabe, K.; Brower-Thomas, T. L.; Kaxiras, E.; Kim, P. Heterointerface effects in the electrointercalation of van der Waals heterostructures. *Nature* **2018**, *558*, 425–429.

[56] Zhang, J. S.; Sun, J.; Li, Y. B.; Shi, F. F.; Cui, Y. Electrochemical control of copper intercalation into nanoscale Bi_2Se_3. *Nano Lett.* **2017**, *17*, 1741–1747.

[57] Kolobov, A. V.; Tominaga, J. *Two-Dimensional Transition-Metal Dichalcogenides*; Springer: Cham, 2016.

[58] Kertesz, M.; Hoffmann, R. Octahedral vs. trigonal-prismatic coordination and clustering in transition-metal dichalcogenides. *J. Am. Chem. Soc.* **1984**, *106*, 3453–3460.

[59] Liang, L. B.; Puretzky, A. A.; Sumpter, B. G.; Meunier, V. Interlayer bond polarizability model for stacking-dependent low-frequency Raman scattering in layered materials. *Nanoscale* **2017**, *9*, 15340–15355.

[60] Huang, Q.M.; Wang, L. F.; Xu, Z.; Wang, W. L.; Bai, X. D. *In-situ* TEM investigation of MoS_2 upon alkali metal intercalation. *Sci. China. Chem.* **2018**, *61*, 222–227.

[61] Fan, S. X.; Zou, X. L.; Du, H. D.; Gan, L.; Xu, C. J.; Lv, W.; He, Y. B.; Yang, Q. H.; Kang, F. Y.; Li, J. Theoretical investigation of the intercalation chemistry of lithium/sodium ions in transition metal dichalcogenides. *J. Phys. Chem. C* **2017**, *121*, 13599–13605.

[62] Mortazavi, M.; Wang, C.; Deng, J. K.; Shenoy, V. B.; Medhekar, N. V. *Ab initio* characterization of layered MoS_2 as anode for sodium-ion batteries. *J. Power Sources* **2014**, *268*, 279–286.

[63] Bissessur, R.; Kanatzidis, M. G.; Schindler, J. L.; Kannewurf, C. R. Encapsulation of polymers into MoS_2 and metal to insulator transition in metastable MoS_2. *J. Chem. Soc. Chem. Commun.* **1993**, 1582–1585.

[64] Py, M. A.; Haering, R. R. Structural destabilization induced by lithium intercalation in MoS_2 and related compounds. *Can. J. Phys.* **1983**, *61*, 76–84.

[65] Yang, D.; Frindt, R. F. Li-intercalation and exfoliation of WS_2. *J. Phys. Chem. Solids* **1996**, *57*, 1113–1116.

[66] Gordon, R. A.; Yang, D.; Crozier, E. D.; Jiang, D. T.; Frindt, R. F. Structures of exfoliated single layers of WS_2, MoS_2, and $MoSe_2$ in aqueous suspension. *Phys. Rev. B* **2002**, *65*, 125407.

[67] Tsai, H. L.; Heising, J.; Schindler, J. L.; Kannewurf, C. R.; Kanatzidis, M. G. Exfoliated−restacked phase of WS_2. *Chem. Mater.* **1997**, *9*, 879–882.

[68] Ganal, P.; Olberding, W.; Butz, T.; Ouvrard, G. Soft chemistry induced host metal coordination change from octahedral to trigonal prismatic in 1T-TaS_2. *Solid State Ion.* **1993**, *59*, 313–319.

[69] Wypych, F.; Schöllhorn, R. 1T-MoS_2, a new metallic modification of molybdenum disulfide. *J. Chem. Soc. Chem. Commun.* **1992**, 1386–1388.

[70] Prouzet, E.; Heising, J.; Kanatzidis, M. G. Structure of restacked and pillared WS_2: An X-ray absorption study. *Chem. Mater.* **2003**, *15*, 412–418.

[71] Yang, D.; Jiménez Sandoval, S.; Divigalpitiya, W. M. R.; Irwin, J. C.;

Frindt, R. F. Structure of single-molecular-layer MoS_2. *Phys. Rev. B* **1991**, *43*, 12053–12056.
[72] Qin, X. R.; Yang, D.; Frindt, R. F.; Irwin, J. C. Real-space imaging of single-layer MoS_2 by scanning tunneling microscopy. *Phys. Rev. B* **1991**, *44*, 3490–3493.
[73] Hu, T.; Li, R.; Dong, J. M. A new (2 × 1) dimerized structure of monolayer 1T-molybdenum disulfide, studied from first principles calculations. *J. Chem. Phys.* **2013**, *139*, 174702.
[74] Yu, Y. F.; Nam, G. H.; He, Q. Y.; Wu, X. J.; Zhang, K.; Yang, Z. Z.; Chen, J. Z.; Ma, Q. L.; Zhao, M. T.; Liu, Z. Q. et al. High phase-purity 1T′-MoS_2- and 1T′-$MoSe_2$-layered crystals. *Nat. Chem.* **2018**, *10*, 638–643.
[75] Heising, J.; Kanatzidis, M. G. Structure of restacked MoS_2 and WS_2 elucidated by electron crystallography. *J. Am. Chem. Soc.* **1999**, *121*, 638–643.
[76] Benavente, E.; Santa Ana, M. A.; Mendizábal, F.; González, G. Intercalation chemistry of molybdenum disulfide. *Coord. Chem. Rev.* **2002**, *224*, 87–109.
[77] Wypych, F.; Weber, T.; Prins, R. Scanning tunneling microscopic investigation of 1T-MoS_2. *Chem. Mater.* **1998**, *10*, 723–727.
[78] Heising, J.; Kanatzidis, M. G. Exfoliated and restacked MoS_2 and WS_2: Ionic or neutral species? Encapsulation and ordering of hard electropositive cations. *J. Am. Chem. Soc.* **1999**, *121*, 11720–11732.
[79] Qin, X. R.; Yang, D.; Frindt, R. F.; Irwin, J. C. Scanning tunneling microscopy of single-layer MoS_2 in water and butanol. *Ultramicroscopy* **1992**, *42–44*, 630–636.
[80] Dungey, K. E.; Curtis, M. D.; Penner-Hahn, J. E. Structural characterization and thermal stability of MoS_2 intercalation compounds. *Chem. Mater.* **1998**, *10*, 2152–2161.
[81] Wypych, F.; Solenthaler, C.; Prins, R.; Weber, T. Electron diffraction study of intercalation compounds derived from 1T-MoS_2. *J. Solid State Chem.* **1999**, *144*, 430–436.
[82] Wypych, F.; Weber, T.; Prins, R. Scanning tunneling microscopic investigation of $K_x(H_2O)_yMoS_2$. *Surf. Sci.* **1997**, *380*, L474-L478.
[83] Shannon, R. Revised effective ionic radii and systematic studies of interatomic distances in halides and chalcogenides. *Acta Cryst.* **1976**, *32*, 751–767.
[84] Basu, S.; Worrell, W. L. *Fast Ion Transport in Solids*; Vashishta, P.; Mundy, J. N.; Shenoy, G., Eds.; Elsevier: Amsterdam, 1979.
[85] Kim, N.; Kim, K. S.; Jung, N.; Brus, L.; Kim, P. Synthesis and electrical characterization of magnetic bilayer graphene intercalate. *Nano Lett.* **2011**, *11*, 860–865.
[86] Gallagher, P.; Lee, M.; Petach, T. A.; Stanwyck, S. W.; Williams, J. R.; Watanabe, K.; Taniguchi, T.; Goldhaber-Gordon, D. A high-mobility electronic system at an electrolyte-gated oxide surface. *Nat. Commun.* **2015**, *6*, 6437.
[87] Browning, A.; Kumada, N.; Sekine, Y.; Irie, H.; Muraki, K.; Yamamoto, H. Evaluation of disorder introduced by electrolyte gating through transport measurements in graphene. *Appl. Phys. Express* **2016**, *9*, 065102.
[88] Ovchinnikov, D.; Gargiulo, F.; Allain, A.; Pasquier, D. J.; Dumcenco, D.; Ho, C. H.; Yazyev, O. V.; Kis, A. Disorder engineering and conductivity dome in ReS_2 with electrolyte gating. *Nat. Commun.* **2016**, *7*, 12391.
[89] Couto, N. J. G.; Costanzo, D.; Engels, S.; Ki, D. K.; Watanabe, K.; Taniguchi, T.; Stampfer, C.; Guinea, F.; Morpurgo, A. F. Random strain fluctuations as dominant disorder source for high-quality on-substrate graphene devices. *Phys. Rev. X* **2014**, *4*, 041019.
[90] Wang, L.; Meric, I.; Huang, P. Y.; Gao, Q.; Gao, Y.; Tran, H.; Taniguchi, T.; Watanabe, K.; Campos, L. M.; Muller, D. A. et al. One-dimensional electrical contact to a two-dimensional material. *Science* **2013**, *342*, 614–617.
[91] Enyashin, A. N.; Seifert, G. Density-functional study of Li_xMoS_2 intercalates ($0 \le x \le 1$). *Comput. Theor. Chem.* **2012**, *999*, 13–20.
[92] Somoano, R. B.; Hadek, V.; Rembaum, A. Alkali metal intercalates of molybdenum disulfide. *J. Chem. Phys.* **1973**, *58*, 697–701.
[93] Gregory, T. D.; Hoffman, R. J.; Winterton, R. C. Nonaqueous electrochemistry of magnesium: Applications to energy storage. *J. Electrochem. Soc.* **1990**, *137*, 775–780.
[94] Bruce, P. G.; Krok, F.; Nowinski, J.; Gibson, V. C.; Tavakkoli, K. Chemical intercalation of magnesium into solid hosts. *J. Mater. Chem.* **1991**, *1*, 705–706.
[95] Koski, K. J.; Wessells, C. D.; Reed, B. W.; Cha, J. J.; Kong, D. S.; Cui, Y. Chemical intercalation of zerovalent metals into 2D layered Bi_2Se_3 nanoribbons. *J. Am. Chem. Soc.* **2012**, *134*, 13773–13779.
[96] Xi, X. X.; Zhao, L.; Wang, Z. F.; Berger, H.; Forró, L.; Shan, J.; Mak, K. F. Strongly enhanced charge-density-wave order in monolayer $NbSe_2$. *Nat. Nanotechnol.* **2015**, *10*, 765–769.
[97] Klemm, R. A. Pristine and intercalated transition metal dichalcogenide superconductors. *Phys. C: Supercond. Appl.* **2015**, *514*, 86–94.
[98] Hossain, M.; Zhao, Z. Y.; Wen, W.; Wang, X. S.; Wu, J. X.; Xie, L. M. Recent advances in two-dimensional materials with charge density waves: Synthesis, characterization and applications. *Crystals* **2017**, *7*, 298.
[99] Banerjee, A.; Garg, A.; Ghosal, A. Emergent superconductivity upon disordering a charge density wave ground state. *Phys. Rev. B* **2018**, *98*, 104206.
[100] Lian, C. S.; Si, C.; Wu, J.; Duan, W. First-principles study of Na-intercalated bilayer $NbSe_2$: Suppressed charge-density wave and strain-enhanced superconductivity. *Phys. Rev. B* **2017**, *96*, 235426.
[101] Wang, X. F.; Shen, X.; Wang, Z. X.; Yu, R. C.; Chen, L. Q. Atomic-scale clarification of structural transition of MoS_2 upon sodium intercalation. *ACS Nano* **2014**, *8*, 11394–11400.
[102] Hui, J. S.; Burgess, M.; Zhang, J. R.; Rodríguez-López, J. Layer number dependence of Li^+ intercalation on few-layer graphene and electrochemical imaging of its solid–electrolyte interphase evolution. *ACS Nano* **2016**, *10*, 4248–4257.
[103] Song, M. K.; Hong, S. D.; No, K. T. The structure of lithium intercalated graphite using an effective atomic charge of lithium. *J. Electrochem. Soc.* **2001**, *148*, A1159–A1163.